

An improved model of the lightning electromagnetic field interaction with the D-region ionosphere

R. A. Marshall¹

Received 23 November 2011; revised 9 January 2012; accepted 16 January 2012; published 14 March 2012.

[1] We present an improved time-domain model of the lightning electromagnetic pulse (EMP) interaction with the lower ionosphere. This improved model inherently accounts for the Earth's curvature, includes an arbitrary number of ion species, and uses a convolutional Perfectly Matched Layer (PML) boundary. We apply an improved model of electron heating due to the lightning EMP and electrostatic fields, and we include ionization, attachment, and detachment. In addition to modeling lightning, this model can be used for long-distance VLF wave propagation in the Earth-ionosphere waveguide, heating of the lower ionosphere by VLF transmitters, and heating in the F-region ionosphere by lightning. In this paper we present three initial results of this model. First, we compare results of ionospheric heating and electron density disturbances with and without electron detachment taken into account. We find that detachment is important only for the QE effects on time scales longer than 1 ms. Second, we find a simple explanation for the recently-reported “elven doublets”, which we find are an effect of the rise and fall times of the lightning waveform. In particular, we find that all elves are doublets, and the rise and fall times of the current pulse control the brightness and separation in time of the two successive halves of the elve. Third, we find a similar simple explanation for “ring” sprites, whole columns appear in a circle symmetric around the discharge axis. We find that ring sprites can be initiated for particular current waveforms, where the QE and EMP fields in the mesosphere produce a maximum reduced field away from the discharge axis.

Citation: Marshall, R. A. (2012), An improved model of the lightning electromagnetic field interaction with the D-region ionosphere, *J. Geophys. Res.*, 117, A03316, doi:10.1029/2011JA017408.

1. Introduction

[2] Lightning discharges produce both an electromagnetic pulse (EMP), due to the rapid lightning current pulse, which radiates primarily in the Very Low Frequency (VLF) part of the spectrum [e.g., *Cummer et al.*, 1998], as well as a quasi-electrostatic (QE) field due to the removal of charge from the thundercloud. When the QE field exceeds the breakdown threshold E_k , sprites can be initiated in the mesosphere [e.g., *Pasko et al.*, 1997]. In addition, the QE field leads to heating, ionization, and optical emissions known as “sprite halos” in the D-region ionosphere at 85–90 km altitude [e.g., *Barrington-Leigh et al.*, 2001]; the EMP field similarly leads to heating, ionization, and optical emissions referred to as “elves” [*Fukunishi et al.*, 1996]. The physical mechanism for halos and elves appears to be the same, but as they are excited by different parts of the lightning electromagnetic field, they operate on different time scales and have different physical shapes.

[3] Measurement of the lightning-induced heating and ionization in the D-region has so far been restricted to sub-ionospheric VLF [e.g., *Inan et al.*, 2010] and MF [*Farges et al.*, 2007; *Farges and Blanc*, 2011] remote sensing. In the VLF method, a ground-based VLF transmitter signal propagating in the Earth-ionosphere waveguide is monitored, and its amplitude and phase measured at some receiver site is sensitive to small variations in the D-region conductivity. The amplitude and phase perturbation to this VLF signal, however, do not have a simple relationship to the D-region electron density disturbance [*Marshall and Inan*, 2010].

[4] Accurate measurements of lightning-induced heating and ionization in the D-region requires a robust model of the lightning-ionosphere interaction. Using such a model, the measured optical signature (elves, halos, or both) can be directly related to heating and ionization through the model outputs of those quantities. For example, the lightning-induced ionization has been inferred through spectral measurements of elves from space [*Mende et al.*, 2005] by estimating the electric field magnitude in the D-region. In addition, model results can be used with studies of sub-ionospheric VLF perturbations (“Early VLF” events [e.g., *Haldoupis et al.*, 2006]) to estimate the relationship between

¹Department of Electrical Engineering, Stanford University, Stanford, California, USA.

the VLF perturbation and the D-region disturbance in a statistical sense.

[5] A number of previous models have been developed in the past ~ 20 years to address these problems. *Taranenko et al.* [1993] presented the first time domain 1D model of the EMP interaction with the ionosphere, and predicted heating, ionization, and optical emissions which would later be verified as elves. *Pasko et al.* [1997] used a 2D cylindrically-symmetric model to study the QE field and its effects in the D-region, inadvertently predicting sprite halos. *Veronis et al.* [1999] created a 2D cylindrical model of the EMP and calculated both sprite halo and elve effects simultaneously. Other 2D models have been presented by *Cho and Rycroft* [1998] and *Rowland et al.* [1995, 1996]. The first 3D models were presented by *Cho and Rycroft* [2001] and *Nagano et al.* [2003]. Finally, *Marshall et al.* [2008, 2010] used a 3D model in cartesian coordinates to investigate the effects of horizontal lightning discharges and the dip angle of Earth's magnetic field.

[6] In this paper, we present a new model of the lightning-ionosphere interaction. This new model attempts to include the most important aspects of previous models, but also makes some improvements and includes a number of features that were previously neglected. In the next section we describe this new model and its salient features.

2. Model Description

[7] We employ a new finite-difference time-domain (FDTD) model of the lightning-ionosphere interaction. This model solves the same three fundamental equations as prior models [e.g., *Marshall et al.*, 2010], namely Maxwell's equations and the Langevin equation:

$$\epsilon_0 \frac{\partial \mathbf{E}}{\partial t} = \nabla \times \mathbf{H} - \mathbf{J}_{\text{tot}} \quad (1)$$

$$\mu_0 \frac{\partial \mathbf{H}}{\partial t} = \nabla \times \mathbf{E} \quad (2)$$

$$\frac{\partial \mathbf{J}_n}{\partial t} + \nu_n \mathbf{J}_n = \vec{\omega}_{c,n} \times \mathbf{J}_n + \omega_{p,n}^2 \epsilon_0 \mathbf{E} \quad (3)$$

where we include up to n charged species, and $\mathbf{J}_{\text{tot}} = \sum_n \mathbf{J}_n$. The vector gyrofrequency $\vec{\omega}_{c,n} = q_n \mathbf{B}_0 / m_n$ is species and magnetic-field dependent, as is the plasma frequency $\omega_{p,n} = (q_n^2 N_n / m_n \epsilon_0)^{1/2}$. The collision frequency ν_n is between species n and the neutral air. \mathbf{B}_0 is the vector geomagnetic field, and q_n , m_n and N_n are the charge, mass, and number density, respectively, of species n .

[8] Maxwell's equations are solved using leapfrog centered-differences as in the traditional Yee algorithm [Yee, 1966], but in a spherical coordinate system. The center of the Earth is taken as the origin, and we model in radius from R_E to $R_E + h$. The 2D version of the model uses the $\theta = 0$ axis as the axis of symmetry, in which case the source is located at the "north pole", and the system is symmetric in ϕ . This coordinate system allows us to use a 2D system when appropriate, but include the effects of the curvature of the Earth naturally. Updating the E_r component on the $\theta = 0$ axis

requires a correction that is similar to the axial correction in cylindrical coordinates; the primary difference is that Ampère's law is applied over a small "cap" with angular extent $\Delta\theta/2$; in this way, the on-axis E_r depends only on its neighboring H_ϕ according to:

$$E_r|_{i+1/2,j=0}^{n+1} = C_{1e} E_r|_{i+1/2,j=0}^n + C_{2e} \frac{\sin\theta_{j=1/2}}{r_{i+1/2}(1 - \cos\theta_{j=1/2})} H_\phi|_{i+1/2,j=1/2}^{n+1/2} \quad (4)$$

where C_{1e} and C_{2e} are constants which depend on Δr , $\Delta\theta$, and Δt .

[9] For the 3D version of the model, a spherical coordinate system with a source at the north pole leads to very small grid cells (in the ϕ dimension) near the source, and extremely large grid cells far from the source. To force the grid cells to have nearly uniform size but keep the curvature of the Earth, we move the source in the 3D version to a location on the "equator", so that θ runs from $\pi/2 - R_E/d$ to $\pi/2 + R_E/d$, where d is the maximum range of interest; and ϕ runs from $-R_E/d$ to R_E/d . The grids used in the 2D and 3D models are shown in Figure 1. In addition to the spherical coordinate system, we employ a variable grid cell size in radius, in order to capture the smaller wavelengths in the ground and the ionosphere. In the simulations shown here, Δr is 100 m in the ground, 1 km in air, and either 500 m or 200 m (user selectable) above 70 km altitude.

[10] The Langevin equation is solved using the method of *Lee and Kalluri* [1999]. In this method, all three \mathbf{J} components are placed at integer grid locations, and at the same time step as \mathbf{E} . This choice results in a simple, fully explicit algorithm with minimal spatial averaging; however, it remains subject to the strict stability criterion in a magnetized plasma, that the time step is restricted by the faster propagating mode [Lee and Kalluri, 1999].

[11] The model allows for any time- and space-varying input current densities J to be applied as a source. For the simulations shown here, the lightning current waveform is defined by a linear rise to its maximum value in time τ_r , and an exponential decay back to zero with time constant τ_f :

$$J_s(t) = \begin{cases} J_0 t / \tau_r & t < \tau_r \\ J_0 e^{-(t-\tau_r)^2 / \tau_f^2} & t \geq \tau_r \end{cases} \quad (5)$$

[12] Note that the equation defines the current density; this current density is distributed over a region of a few grid cells (in θ in 2D, and in both θ and ϕ in the 3D version) in order to reduce numerical dispersion, as in the work of *Veronis et al.* [1999]. The peak current I_k is then determined by integrating J_s over this small region.

[13] The simulation space is truncated with a Convolutional Perfectly Matched Layer boundary (CPML [Roden and Gedney, 2000]), which is independent of the medium. In a traditional PML [Bérenger, 1994], an artificial layer of absorbing material a few cells thick is used to attenuate waves reaching the simulation boundary. However, in the anisotropic magnetized plasma above ~ 80 km, the CPML behaves poorly for waves propagating nearly parallel to \mathbf{B}_0 and grazing the boundary. This problem was noted by

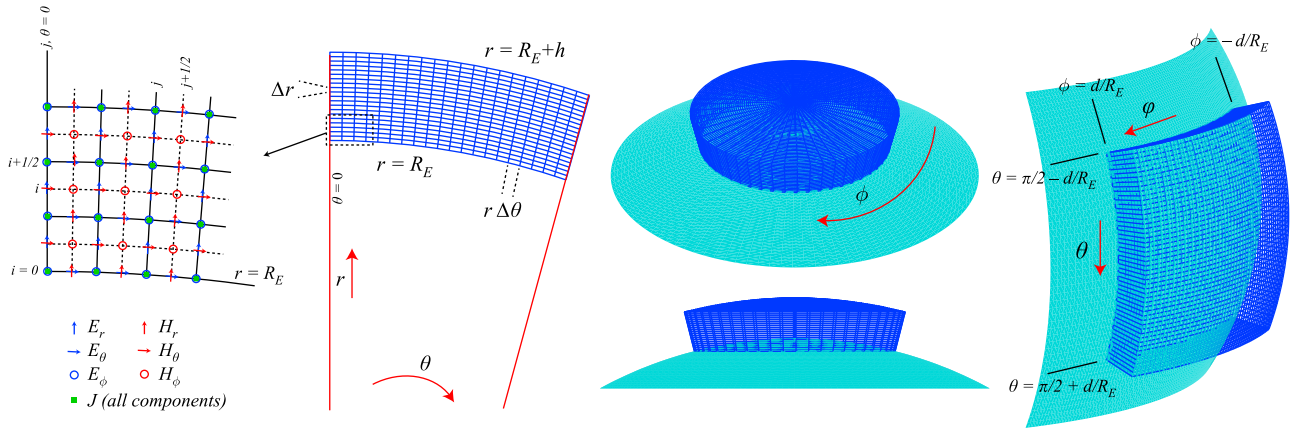


Figure 1. (left) Two-dimensional spherical grid. The left edge is the $\theta = 0$ axis. (middle) Extrapolating the 2D grid from the left to 3D leads to very small grid cells near the north pole. (right) The alternative 3D grid, which is centered on the equator, has grid cells of nearly constant size.

Becache et al. [2003] and *Chevalier et al.* [2008]; in short, while the group velocity vector has a component towards the boundary, the phase velocity vector has a component pointing away from the boundary, and since the CPML works to attenuate in the direction of phase propagation, the wave is amplified. This instability appears at the far boundary of the 2D simulation at ~ 85 km altitude; to avoid it, we stop the simulation when the radiated EMP reaches this altitude at the far boundary.

2.1. Ionosphere and Atmosphere

[14] The VLF wave interaction with the D-region ionosphere is primarily controlled by the electron and neutral particle densities, and to a lesser extent by the ion densities and the Earth’s magnetic field. Electron density profiles are taken from the International Reference Ionosphere (IRI)

2007 model [*Bilitza and Reinisch, 2008*]; example profiles are shown in Figure 2. For comparison, we also show the traditional exponential profile from *Wait and Spies* [1964] with $h' = 84.2$ km and $\beta = 0.5$. This profile is only useful below 90 km altitude, and generally yields a shallower gradient in the D-region compared to the IRI model.

[15] We use neutral density profiles from the MSIS-E-90 model [*Hedin, 1991*], also shown in Figure 2. The relative number densities are important inputs into the kinetic calculations of electron mobility and ionization and attachment rates in the next section. Previous models have assumed a simple atmosphere of 78% N_2 , 21% O_2 , and 1% Argon; however, such an atmosphere is only valid below 100 km altitude.

[16] Similar to *Hu and Cummer* [2006], in the present simulations, equation (3) above use a single positive ion

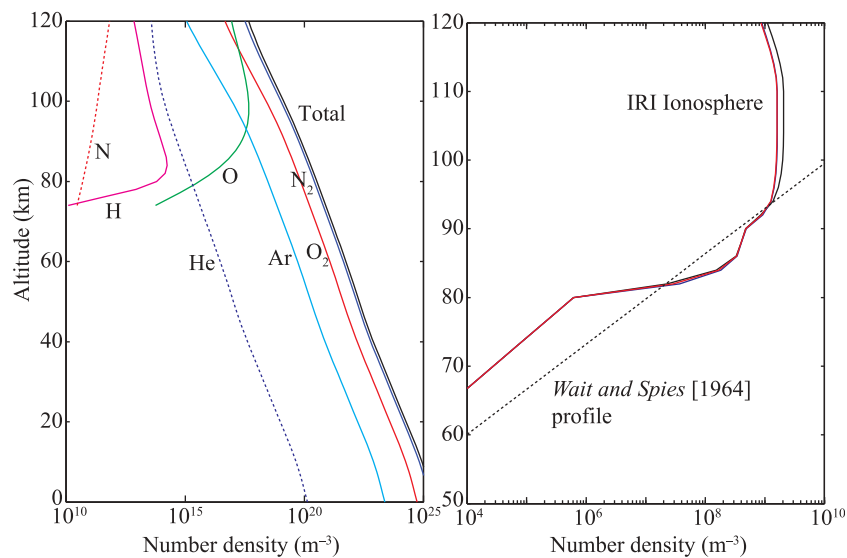


Figure 2. (left) Neutral density profiles, including atmospheric constituents; from MSIS-E-90 model [*Hedin, 1991*]. (right) Nighttime electron density profiles, taken from IRI model 2007 [*Bilitza and Reinisch, 2008*] and the traditional exponential model [*Wait and Spies, 1964*] for comparison.

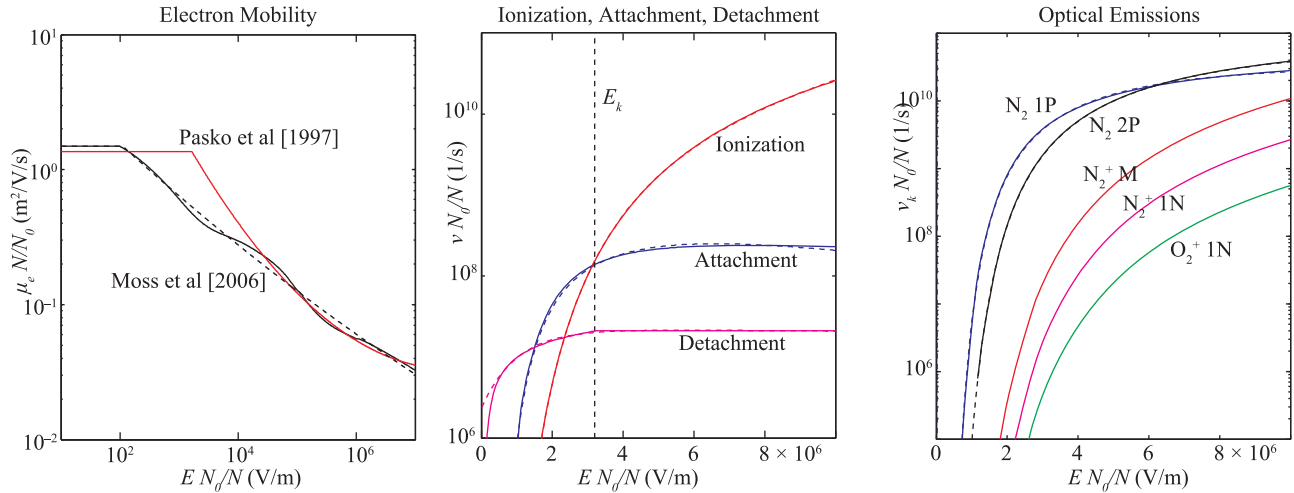


Figure 3. (left) Electron mobility as a function of local electric field, comparing the profile used by *Pasko et al.* [1997] to the rates calculated by *Moss et al.* [2006]. In the present work we use an analytical fit to the Moss et al. rate, shown as a dashed line. (middle) Ionization, dissociative attachment, and associative detachment rates from Moss et al. and *Luque and Gordillo-Vázquez* [2011] (solid lines), and analytical fits used here (dashed). (right) Optical excitation rates from *Moss* and analytical fits.

species with a density profile identical to that of electrons; except where the electron density is below 100 cm^{-3} , the ion density is held to this constant value. The ion collision frequency is assumed to be 100 times less than that of electrons. The ion mass is taken to be that of NO^+ , the dominant positive ion above 80 km [*Kopp*, 1992]. Below 80 km, the dominant positive ions are proton hydrates $\text{H}^+(\text{H}_2\text{O})_n$; however we neglect these ions since most of the nonlinear effects described below occur above 80 km. The model can include any number of ion species, with specified mass, charge, and density and collision frequency profiles, but each ion species adds $\sim 15\%$ to the model run time.

2.2. Nonlinear Effects

[17] As in prior models of the lightning EMP, we calculate an ensemble of nonlinear effects in the D-region ionosphere, including heating, ionization, attachment, and optical emissions. In addition, in this new model we include the effects of collisional electron detachment from O^- , which dominates over attachment and ionization at low electric fields ($EN_0/N < 1.5 \times 10^6 \text{ V/m}$). We will investigate the effects of detachment in section 3.

[18] The rate coefficients used for detachment, attachment, and ionization are shown in Figure 3; for comparison, we also show the rate coefficients calculated by *Moss et al.* [2006]. Therein, the authors used a Monte Carlo model to determine the electron distribution, and compared their results to calculations using the ELENDF Boltzmann code [*Morgan and Penetrante*, 1990]. Here, we use another Boltzmann solver known as BOLSIG+ [*Hagelaar and Pitchford*, 2005] to calculate the rate coefficients, using cross sections from *Phelps and Pitchford* [1985] and *Lawton and Phelps* [1978]. Like ELENDF, BOLSIG+ solves the Boltzmann equation with a two-term spherical harmonic expansion, and is capable of including electron-electron collisions and AC electric fields.

[19] Each of these rates is updated based on the “effective” electric field E_{eff} , defined as

$$E_{\text{eff}} = E_{\parallel} + E_{\perp} \left(\frac{\nu_{en}^2}{\nu_{en}^2 + \omega_{ce}^2} \right) \quad (6)$$

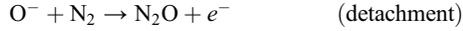
where E_{\parallel} and E_{\perp} are the components of E parallel and perpendicular to B_0 , and ν_{en} is the electron-neutral collision frequency. As mentioned earlier, these rate coefficients are only valid in “air”, where the gas composition is as described above. For altitudes above 100 km, we use BOLSIG+ to calculate new rate coefficients for different gas mixtures, as determined from Figure 2.

3. Electron Detachment

[20] Recent work on the quasi-electrostatic (QE) field interaction with the mesosphere has shown that electron detachment may play a prominent role in the heating and ionization processes that lead to sprite halos and sprites. *Gordillo-Vázquez* [2008], *Gordillo-Vázquez and Luque* [2010], and *Luque and Gordillo-Vázquez* [2011] have shown that detachment plays a key role in sprite ignition, and in particular for delayed sprites. *Liu* [2012] showed that detachment significantly reduces the electron “hole” associated with attachment over timescales of 5 ms or greater. *Neubert et al.* [2011] included detachment in their analysis of the electric fields associated with a complex gigantic jet event. In this section, we investigate the effects of detachment on the QE and EMP fields’ interaction with the ionosphere.

[21] The dominant detachment process at high altitudes is thought to be collisional detachment to N_2 , which occurs in conjunction with dissociative attachment:





[22] The rate coefficients for attachment and detachment are shown in Figure 3. The detachment rate is the same as that used by *Luque and Gordillo-Vázquez* [2011]. While detachment requires a lower electric field threshold and thus dominates at lower fields, clearly it requires the existence of O^- ions, which are negligible in ambient conditions. However, once the field increases past the threshold of attachment, O^- ions produced by attachment can be removed by detachment and the electrons released. The attachment “hole” that has been previously postulated [*Taranenko et al.*, 1993; *Marshall et al.*, 2008] may not be as considerable as previously thought.

[23] We include detachment in the present model through a set of two coupled state equations for the electron and O^- ion density:

$$\frac{\partial N_e}{\partial t} = (\nu_i - \nu_a)N_e + \nu_d N_{\text{O}^-} \quad (7)$$

$$\frac{\partial N_{\text{O}^-}}{\partial t} = \nu_a N_e - \nu_d N_{\text{O}^-} \quad (8)$$

where ν_i , ν_a , and ν_d are the ionization, attachment, and detachment rates, respectively; these rates in turn depend on the local electric field magnitude as shown in Figure 3. To ensure stability, we solve this set of coupled equations using implicit backward Euler time integration. After writing the difference equations in matrix form $A\mathbf{x} = \mathbf{b}$, The numerical update equations are then:

$$\begin{bmatrix} N_e \\ N_{\text{O}^-} \end{bmatrix}^{t+\Delta t} = \frac{1}{|A|} \begin{bmatrix} 1 + \nu_d \Delta t & \nu_a \Delta t \\ \nu_d \Delta t & 1 - \nu_{ia} \Delta t \end{bmatrix} \begin{bmatrix} N_e \\ N_{\text{O}^-} \end{bmatrix}^t \quad (9)$$

where $\nu_{ia} = \nu_i - \nu_a$ and $|A| = 1 - (\nu_{ia} - \nu_d)\Delta t - \nu_i \nu_d \Delta t^2$ is the determinant of the original multiplying matrix. An added benefit of this method is that the model monitors the O^- density as a function of time in addition to the electron density. Equations (9) are solved self-consistently with the field update equations (1)–(3).

[24] Figure 4 shows an example model output where the effects of detachment have been included. This simulation used a 150 kA peak source current from 6 km altitude, with $\tau_r = 40 \mu\text{s}$ and $\tau_f = 80 \mu\text{s}$. The left column shows outputs at $t = 0.608 \text{ ms}$; the right column shows the same outputs at $t = 1.292 \text{ ms}$. This simulation uses a time step of $0.1 \mu\text{s}$. The top panels show the E_r electric field component; in our spherical coordinates, the radial direction is vertical on this plot. The second panels show E_{eff}/E_k , the effective electric field scaled to the breakdown field. Note that the breakdown field is defined as the electric field intensity where $(\nu_i + \nu_d - \nu_a) = 0$, based on the rates in Figure 3, and is thus affected by the inclusion of detachment. Contours show where $E_{\text{eff}} = 0.1E_k$ and $0.01E_k$. In this simulation, the effective field reached a maximum of $1.14E_k$. The next three panels show the O^- ion density produced through attachment, the change in electron density as a percent of the local background density, and the

spatially-integrated energy dissipated through Joule heating. For this latter measurement, we compute $\mathbf{J} \cdot \mathbf{E}$ at each point in the grid, yielding the power density dissipated in Watts/m^3 ; this is then integrated in time and in 3D space, after extrapolating the 2D simulation around the $\theta = 0$ axis. The result in Figure 4 is thus the energy dissipated, in Joules, in an annulus formed by each pixel of the image. The sum of this 2D image yields the total energy dissipated, which in this example is $\sim 6 \text{ MJ}$; integration of the current pulse shows that the charge removed by this discharge is $\sim 13.5 \text{ C}$. This can be compared to the total energy dissipated by a cloud-to-ground discharge, which is estimated by *Cooray* [1997] to be on the order of 500 MJ for a 5 C charge removal.

[25] For the change in electron density, the results here agree with previous modeling work [e.g., *Barrington-Leigh et al.*, 2001; *Marshall et al.*, 2010]. For these parameters, very little ionization is produced, and there is primarily a loss of electrons through attachment, with a maximum near 10% change. This largest change occurs just below 80 km altitude directly above the discharge, and is thus due to the QE field produced by charge removal from the thundercloud. The EMP part of the field produces only 2–3% changes in electron density, out to $\sim 200 \text{ km}$ range. For the O^- density, we see production of as high as 10^7 ions/m^3 . However, in this region the electron density is $\sim 10^9 \text{ m}^{-3}$, and so the peak O^- production is only about 1% of the background electron density.

[26] To investigate the effects of detachment, we run a series of simulations with and without detachment included. The rise time τ_r of the input current waveform is varied between 20 and 70 μs , and the fall time τ_f between 40 and 140 μs ; these simulations use a peak current of 200 kA from 6 km altitude. To allow effects of detachment to accumulate, the simulations are run out to 5 ms. Figure 5 shows results of this series of simulations. The top panel shows the total electron production; the second panel shows the total O^- production; and the third panel shows the total energy dissipated through Joule heating; each of these integrated over the volume to yield a total. These simulations were extended out to 1500 km range to ensure that all effects are captured. The bottom panel in Figure 5 shows the charge moment calculated for each source discharge. For comparison, charge moments calculated by *Cummer and Lyons* [2004] for the first 2 ms of the discharge show that the vast majority of both +CG and –CG discharges have charge moments between 0 and 100 C-km, with rare +CG charge moments up to 500 C-km. Reported charge moments up to 1000’s of C-km included continuing current, which is not included in these simulations.

[27] A few observations can be made from Figure 5. First, as expected, the fastest rise times and fall times produce the highest electron density, O^- , and energy dissipation, simply because the electric field is proportional to dI/dt . However, these are actually the smallest charge moments for the same peak current. As such, while charge moment is an excellent indicator of sprite production [*Hu et al.*, 2002; *Cummer and Lyons*, 2005], it is not a good indicator of ionospheric effects of lightning such as heating, ionization, and elves. Second, note that only the fastest $< 40 \mu\text{s}$ rise times produce net ionization in the first few ms; the slower rise times do not

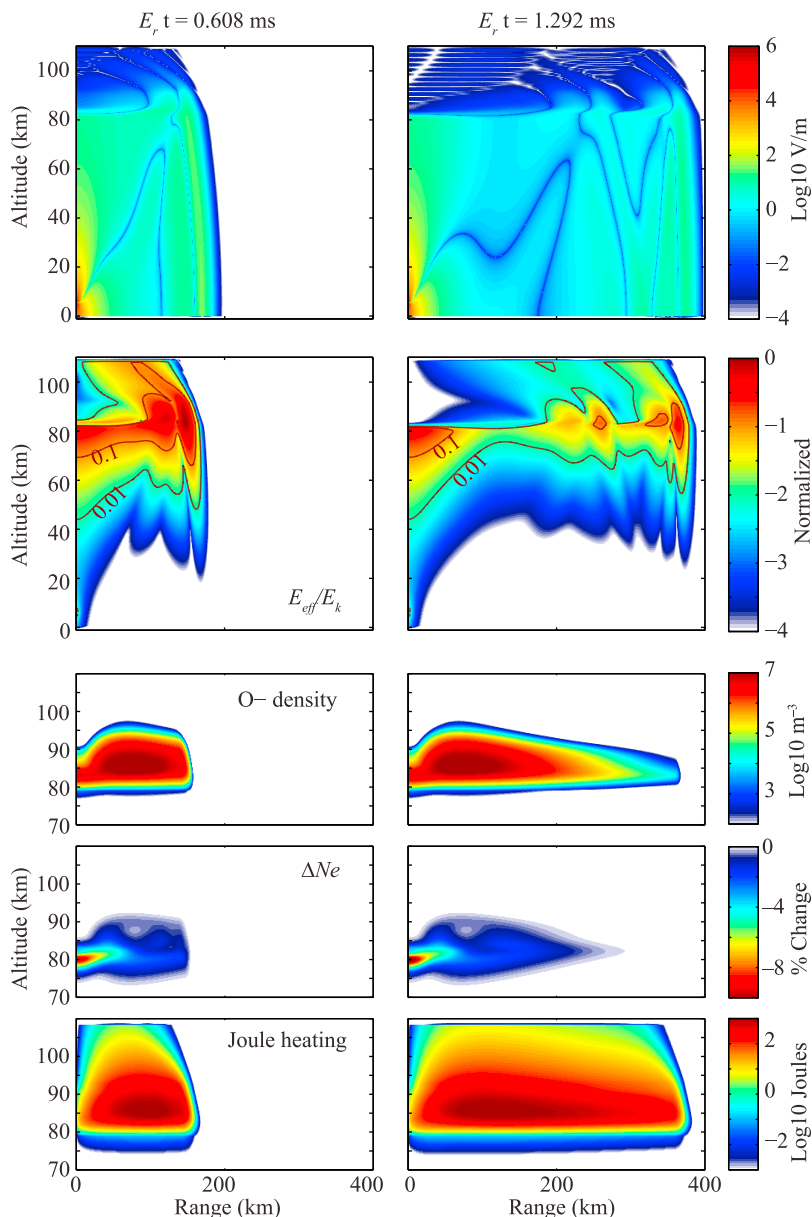


Figure 4. Example simulation with detachment included. See the text for explanation of the various panels.

produce fields large enough to exceed the breakdown field, even for this 200 kA, 6 km discharge.

[28] While barely visible on this plot, there are dashed curves which show the results with detachment turned off. For the electron production, these dashed curves sit just below their solid counterparts: detachment serves to slightly increase the electron production, by counteracting attachment. The difference, however, is less than 0.5% for electrons and $\sim 2\%$ for O^- ions. The effects of detachment on heating are negligible: the change in energy dissipated is less than 0.01%, and is larger for longer rise and fall times. However, the plots in Figure 5 are integrated over the entire volume, and do not tell the entire story. Figure 6 shows the difference in electron density with and without detachment (i.e., $N_e|_{\text{detach}} - N_e|_{\text{nodetach}}$) for three of the simulations:

$\tau_r = 40 \mu\text{s}$, and $\tau_f = 60, 100,$ and $140 \mu\text{s}$. The three top panels show that there is a very small change in electron density for each simulation in the “elve” region, i.e., above 80 km altitude and out to 200 km range. However, in the “QE” region, at about 80 km altitude on the axis, there is an appreciable difference in electron density, which is significant for longer fall times $< 100 \mu\text{s}$. The bottom panel shows the electron density profile after the simulation above the discharge for these three cases. In the absence of detachment, there is a large electron “hole” produced by attachment; but when detachment is included this hole is mostly filled-in in the first 5 ms. This result agrees with *Liu* [2012].

[29] Note that our model is not able to capture the complete effects of detachment, as it does not include

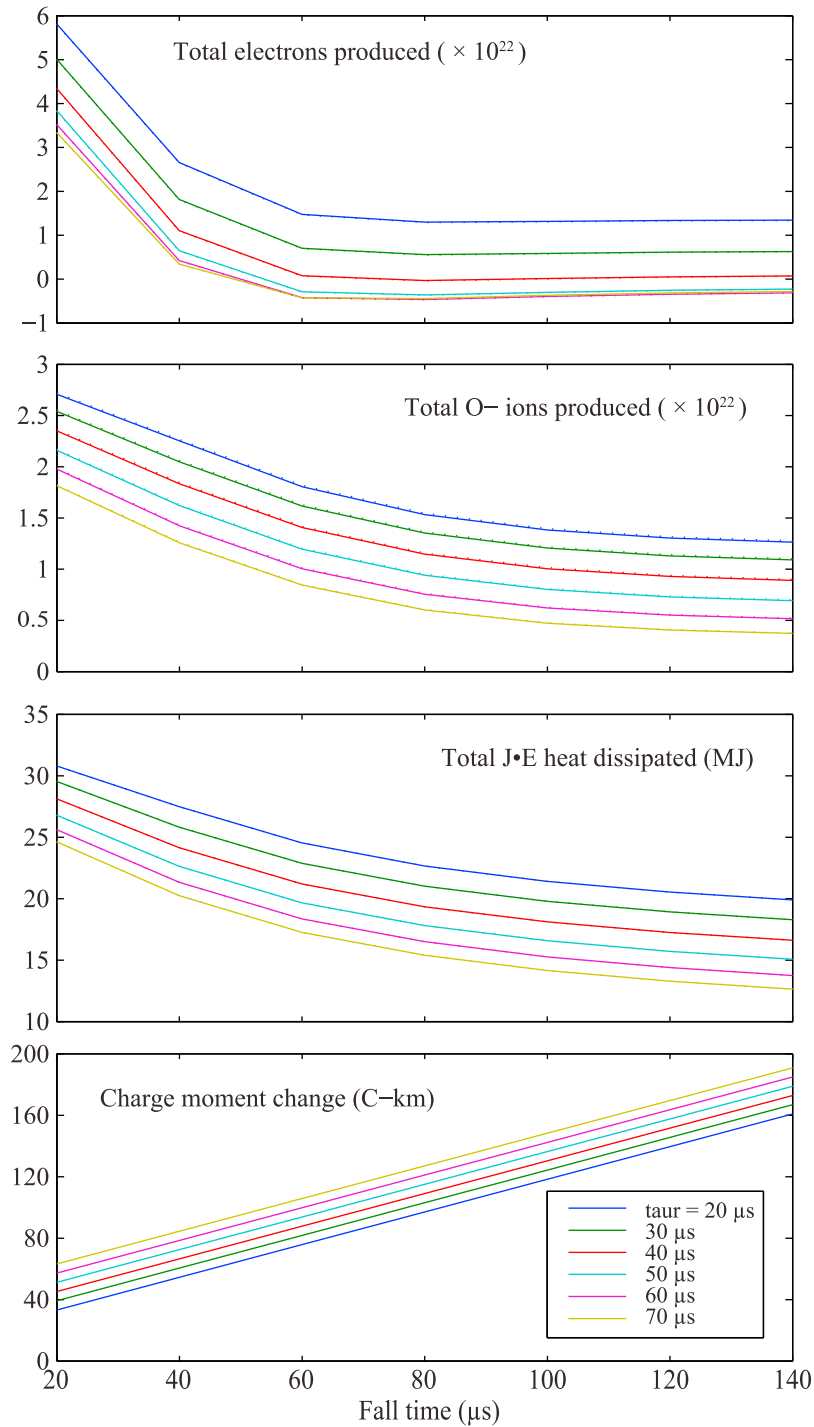


Figure 5. Electron production, O^- ion production, and energy dissipated for different source current waveforms. The bottom panel shows the charge moment change for each waveform. Dashed lines, barely visible, show that the effects with and without detachment included are nearly identical.

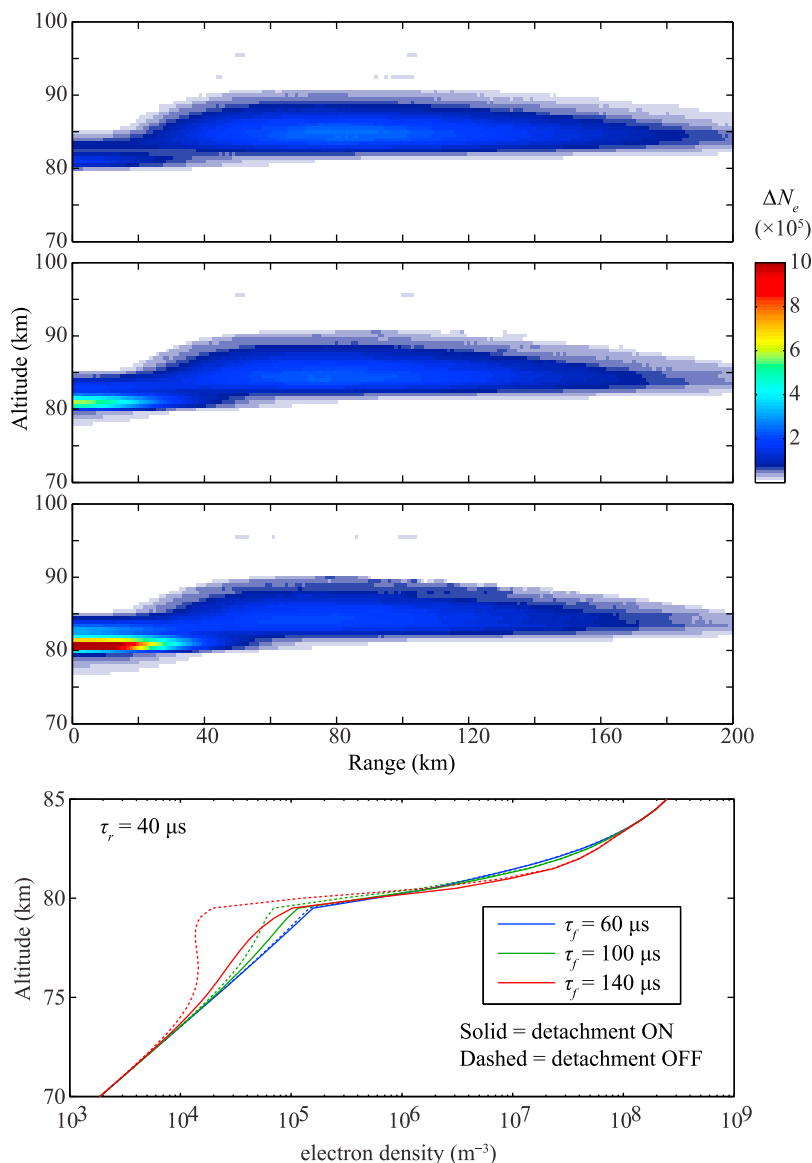


Figure 6. Difference in resulting electron density with and without detachment for three different source current waveforms. The bottom panel shows the difference in electron density along axis above discharge for the same three simulations.

electron transport. As such, the model cannot take into account shielding of the electric field through charge redistribution.

4. Elve Doublets

[30] Reliable ground-based observations of elves are limited to a few summers of observations, due to their short duration of a few hundred μs compared to typical camera speeds of 30 ms exposure. The original elve observations by *Fukunishi et al.* [1996] utilized a high-speed photometric array that could discern the expanding shape of the elve, as predicted by *Inan et al.* [1991]. The “Fly’s Eye” instrument [Barrington-Leigh, 2000] made triggered observations and compared to model outputs using a 2D cylindrical model [Veronis et al., 1999] similar to the present model. More recently, the PIPER instrument [Marshall et al., 2008] has

made continuous observations of elves, without relying on triggering, over the course of entire storms and summer campaigns. *Newsome and Inan* [2010] presented detailed results of elve occurrence rates, and verified the discovery by ISUAL [Chen et al., 2008] that elves occur approximately six times more frequently than sprites.

[31] In the course of PIPER elve observations, a unique type of event was discovered, dubbed an “elve doublet” [Newsome and Inan, 2010]. These events show what appear to be two elves in rapid succession, separated by an average of 120 μs . *Newsome and Inan* [2010] studied a statistical set of 40 elve doublets, and found that every one had a separation between 80 and 160 μs . They argued that these events are unlikely to be caused by multiple return strokes, which would be further separated in time; nor are they due to a ground reflection, which would imply an 18 km altitude source.

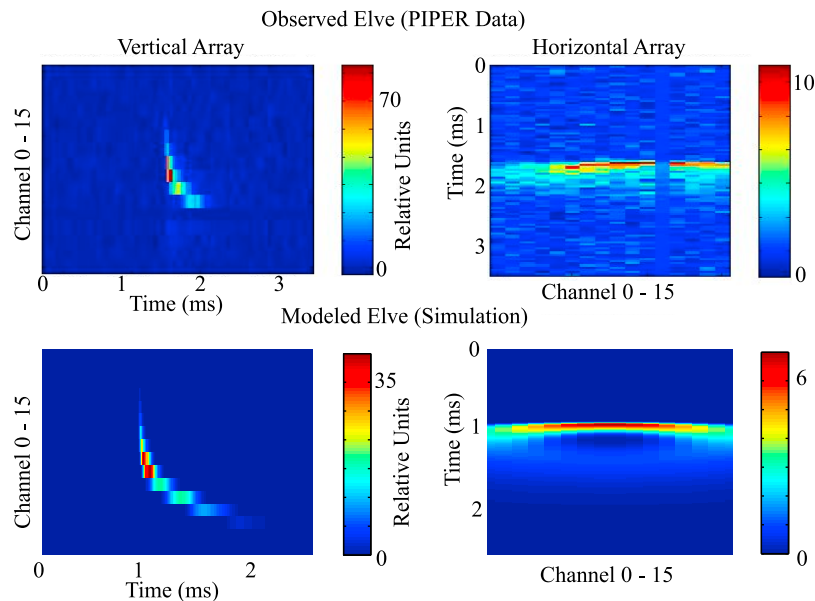


Figure 7. Simulated versus PIPER observed elves.

[32] Using the present model, we seek to provide a simple explanation for these events. We propose that the occurrence of the elve doublet is simply due to the rise and fall of the source current waveform; the radiated field, proportional to dI/dt , exhibits two concentric expanding shells. The observation and separation of the doublet depends on the current rise and fall times and the viewing geometry from the lightning source to the instrument on the ground. It is possible that there is further dependence on ionospheric conditions, but we do not investigate those here.

[33] To investigate the elve doublet effect, we first propagate photons calculated at each time step down to a camera on the ground. To create an elve animation, we initialize a 3D array of 128×128 pixels \times 500 time steps, covering 2 ms (i.e., $4 \mu\text{s}$ resolution). If N photons- $\text{cm}^{-3}\text{-s}^{-1}$ are generated at a given grid cell at time t_1 , then $Ndl\Delta t$ photons- cm^{-2} are placed in the elve animation array at the appropriate camera location, at the time step closest to $t_1 + t_d$, where t_d is the time delay corresponding to the distance between the grid cell and the camera, i.e., $t_d = d/c$, and d is the line-of-sight length through the grid cell as viewed by the camera. An example of the resulting elve animation is provided in the auxiliary material.¹

[34] Next, we average the resulting animation over the 18×18 degree field-of-view of PIPER to produce a space-time image that corresponds to PIPER data. A comparison between actual PIPER data and the 2D model is shown in Figure 7. Not surprisingly, the model reproduces the salient features of the PIPER data extremely well.

[35] To investigate elve doublets, we run a sequence of simulations, varying the lightning current waveform rise and fall times as well as the camera ground location. Figure 8 shows an example of an elve doublet, as viewed by PIPER; an animation of this elve is provided in the auxiliary material. For the simulations shown in this

section, the peak current is held constant at $I_k = 200$ kA from 6 km altitude. The elve shown in Figure 8 and in the auxiliary material is viewed from 400 km range, and uses $\tau_r = 60$ and $\tau_f = 70 \mu\text{s}$. Clearly, these parameters result in an elve doublet, just as measured in PIPER [see Newsome and Inan, 2010]. The lower panel shows the time profile through channel 11 of the vertical array; in this channel, the time between the two peaks is $\sim 80 \mu\text{s}$.

[36] Figure 9 shows the time sequence, similar to Figure 8 (bottom), for a series of simulations, where the rise and fall times of the current waveform have been varied from $20\text{--}70 \mu\text{s}$ and $40\text{--}100 \mu\text{s}$, respectively. In all cases, the camera is located at 400 km. From these simulations we observe a number of interesting features. First, the time of the initial peak of the elve is mostly independent of the rise time, occurring about 1.2 ms after the discharge is initiated. However, the magnitude of the peak is directly related to the rise time: for $\tau_r = 20 \mu\text{s}$, the first peak is 30 MR, while for $\tau_r = 70 \mu\text{s}$, the first peak is only 3 MR. This is directly due to the fact that the radiated field is proportional to dI/dt . Second, the time between the first and second peaks is also directly related to the rise time, increasing for longer rise times. Third, the magnitude of the second peak is directly related to the fall time. In each panel of Figure 9, it is clear that the two peaks are closest in magnitude when the rise and fall times are nearly the same (in fact, they are closest when τ_f is slightly longer than τ_r).

[37] From these results, we can conclude the following about observed elve doublets in PIPER data: First, every elve is a doublet; emissions are triggered by the rising and falling edges of the current waveform. Second, the observation of an elve doublet depends on the time difference between the two peaks and their relative magnitudes. For the most part, a clear elve doublet implies similar rise and fall times of the current waveform, and both must be long enough to separate the two pulses in time.

¹Auxiliary materials are available in the HTML. doi:10.1029/2011JA017408.

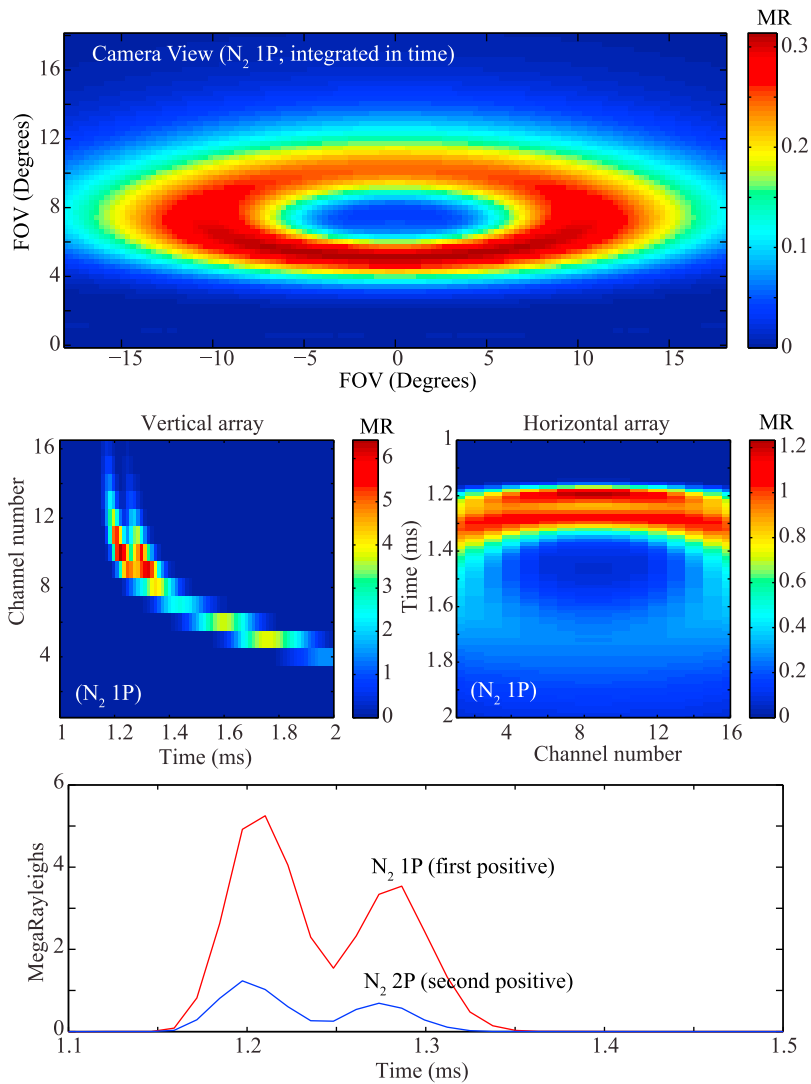


Figure 8. Elve doublet, viewed from 400 km away. In this simulation the rise time is $60 \mu s$ and the fall time is $70 \mu s$. (top) A time-integrated “camera” view; (middle) The PIPER-sampled views. (bottom) Channel #11 of the vertical (middle left) array.

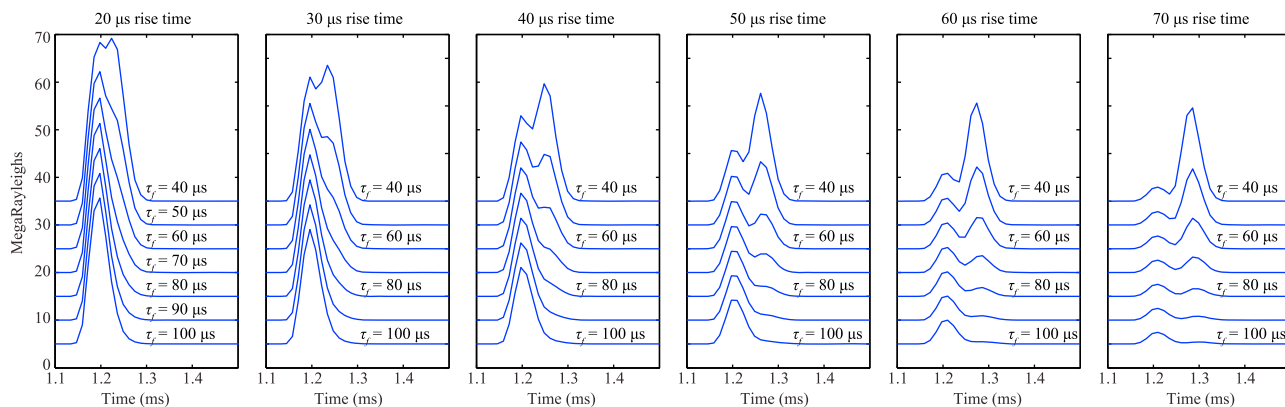


Figure 9. Elve doublets, measured in Channel 11 of the vertical PIPER array (simulated), for varied rise and fall times. The profiles are progressively offset by 5 MR for easy comparison.

[38] Figure 10 quantifies the relationship between the elve doublet peaks and the lightning current parameters. The top panel shows that the magnitude of the first peak is inversely related to the rise time τ_r of the current; however, due to the nonlinear relationship between E_{eff} and the optical emission rates, the relationship is not directly proportional. The magnitude of this first peak is only weakly related to the fall time τ_f . Similarly, the second panel shows that the magnitude of the second peak is inversely related to τ_f , and is only weakly dependent on τ_r . The third panel shows that the time between the two peaks is linearly related to, and almost equal to, τ_r , with weak dependence on τ_f . Note that the actual time difference depends on the PIPER channel under investigation (i.e., the elevation angle). Nonetheless, these results show that with knowledge of the peak current and distance from the discharge, PIPER observations of elves can be used to measure the lightning current waveform in this two-parameter fit.

[39] To investigate the effect of the PIPER viewing location, we repeat this series of simulations, varying the rise and fall times, with a camera located at 500, 600, and 700 km from the discharge. While the shape of the elve changes both in the camera and PIPER views, the salient features of the elve doublets remain the same: the magnitudes of the two peaks are directly related to the rise and fall times, and the time difference between them is directly related to the rise time. This result agrees with PIPER observations: analysis of the ~ 60 elve doublets reported by *Newsome and Inan* [2010] show no preference for distance from the discharge.

5. Ring Sprites

[40] Since their discovery, sprites have been attributed to breakdown in the upper atmosphere caused by the QE field due to lightning. *Hu et al.* [2002], *Cummer and Lyons* [2005], and others have verified this through charge moment measurements of sprite-producing lightning. However, the details of how different types of sprites (“carrot” sprites, “c-sprites”, etc) are produced have not been determined. Here, we propose a mechanism for a type of sprite which we denote “ring” sprites. Reported by *Vadislavsky et al.* [2009], these are c-sprites whose columns appear to be organized in a ring, centered above the discharge. In some cases, carrot sprites appear at the center of the ring. The rings

reported by *Vadislavsky et al.* [2009] have radii of 35–50 km. They proposed a number of possible mechanisms, including “pre-activation” of the mesosphere by the EMP field; or depletion of electrons by attachment due to the EMP field, creating a “hole” absent of electrons directly above the discharge, preventing initiation of a sprite.

[41] Here we present a simpler mechanism for ring sprites, and use the model described herein to investigate. We propose that ring sprites occur due to a combination of the EMP and QE fields due to lightning, whose relative contributions are related to the source lightning current waveform. Typical sprites are produced by the QE field, which can grow to exceed the breakdown threshold through a large charge moment, and has a maximum directly above the discharge. Elves, on the other hand, are produced by the EMP field, which only exceeds the breakdown threshold at ~ 85 km, due to the reduced neutral density. In ring sprites, we suggest that the QE and EMP fields add in the mesosphere to exceed the breakdown threshold. Since the EMP field has a maximum away from the axis, the total field may also have a maximum at some radius away from the discharge.

[42] To investigate this mechanism, we run a series of simulations as above, varying the source current parameters. Figure 11 shows results of two simulations: the top row uses $\tau_r = 20$ and $\tau_f = 40 \mu\text{s}$; the bottom row uses $\tau_r = 60$ and $\tau_f = 140 \mu\text{s}$. Both use 200 kA peak current from 6 km altitude. The first is meant to represent a fast, high- dI/dt discharge, whereas the second represents a slower, higher charge moment discharge. The leftmost panels show a snapshot of the reduced field E_{eff}/E_k at $t = 0.285$ ms. The next panels show slices through the vertical axis (i.e., directly above the discharge), stacked in time to form an image; these have the same structure as similar plots given by *Li et al.* [2008]. The third panels show a similar time-stack plot, where the slice is taken horizontally (in range) at an altitude of $h = 78$ km; for the purposes of this study, we are assuming this to be a likely altitude for sprite initiation [e.g., *Stenbaek-Nielsen et al.*, 2010]. The far right panels show the same slices as the third panels, but stacked up as line plots, where the color of the plot corresponds to time.

[43] We discuss each of these simulations separately, starting with the slower current (bottom panels). From the leftmost panel, we can see the difference immediately: the expanding field has a maximum along the axis in the slower

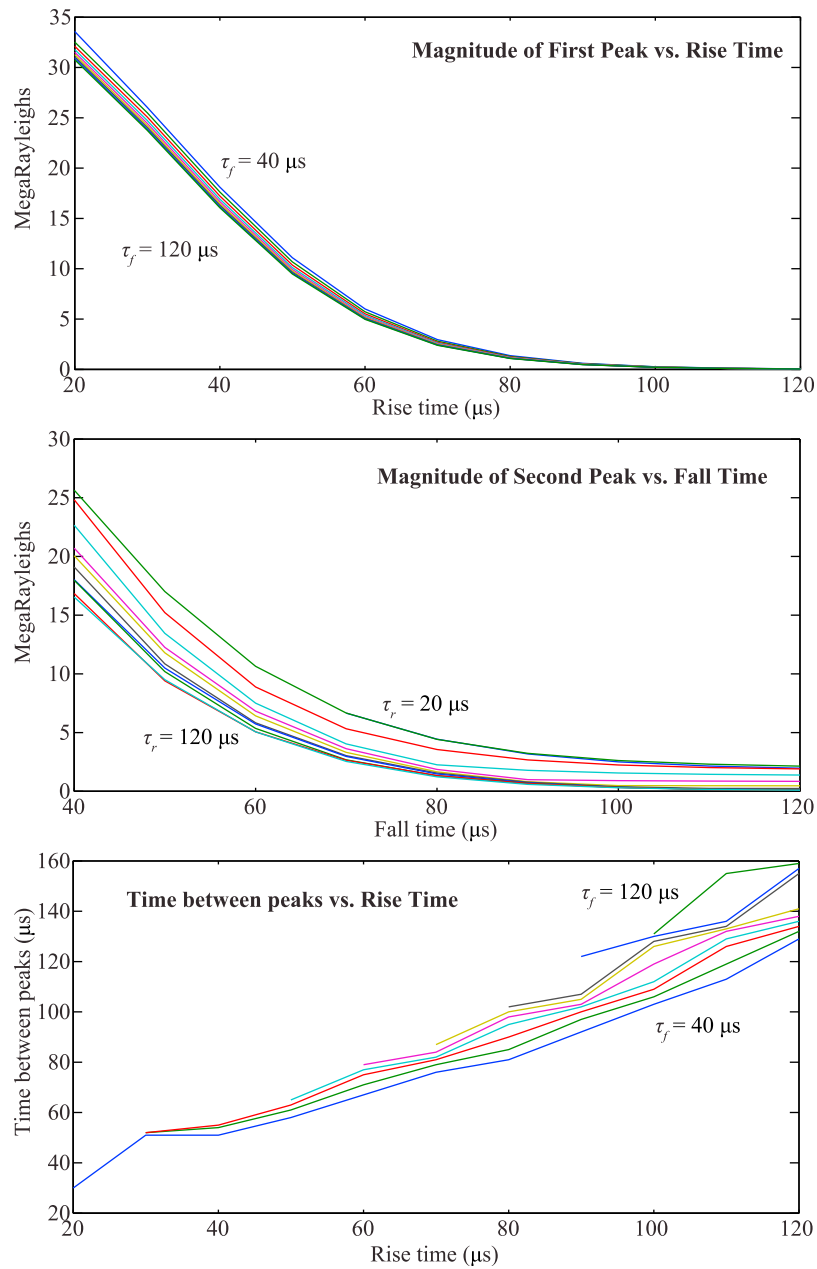


Figure 10. (top) Magnitude of the first peak of an elve doublet with varying τ_r and τ_f . (middle) Same for the second peak. (bottom) Time difference between the two peaks as a function of the time constants. In some of the elves, one of the peaks is washed out by the other, more dominant peak, so a time difference cannot be established.

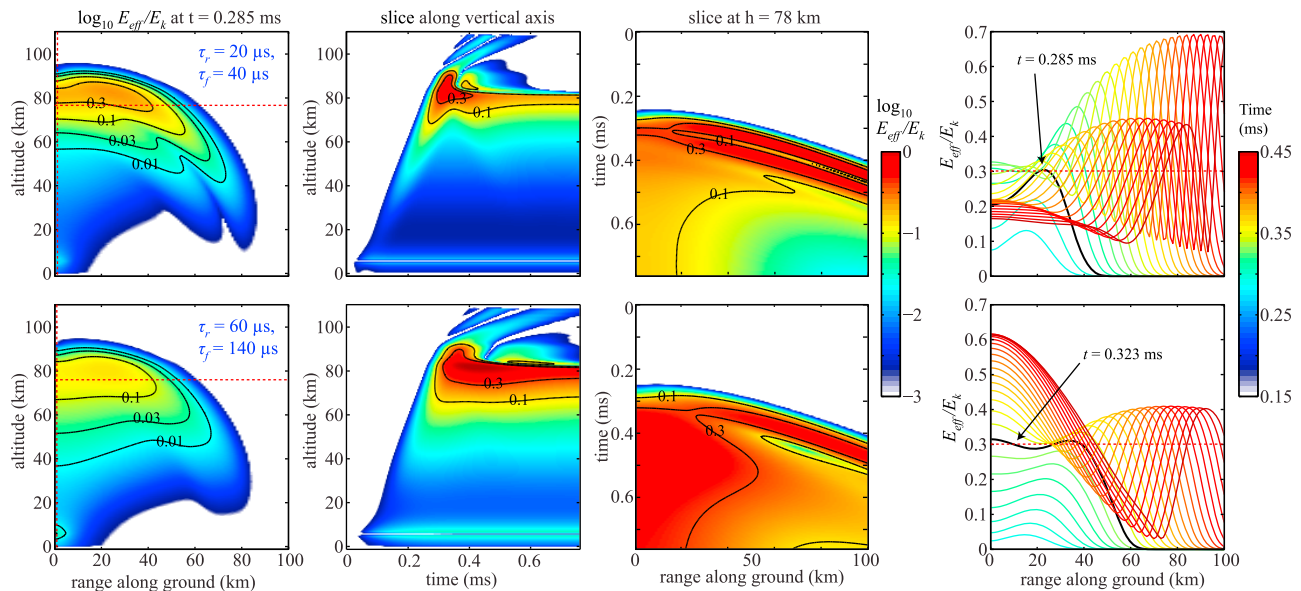


Figure 11. Simulations for two lightning current waveforms using (top) $\tau_r = 20$, $\tau_f = 40$ μs ; and (bottom) $\tau_r = 60$, $\tau_f = 140$ μs . (left to right) Snapshots of E_{eff}/E_k at $t = 0.285$ μs ; image formed of slices through E_{eff}/E_k on the axis, i.e., directly above the discharge, as it evolves in time; image of slices through E_{eff}/E_k through $h = 78$ km, as it evolves in time; and at far right, line plots of those slices through $h = 78$ km. See text for discussion.

(bottom) simulation. The second panel shows that the maximum reduced field is achieved ~ 0.3 ms after the discharge, at about 80 km altitude, and persists for the time duration shown. When continuing current is present, this field can continue to be enhanced; however, conductive shielding of the field also occurs on time scales of ~ 1 ms [Pasko *et al.*, 1997]. The third and fourth panels together show that the maximum reduced field occurs on the axis after the first 0.25 ms. Note that in these simulations the field never reaches the breakdown field E_k ; however, Li *et al.* [2008] demonstrate that sprites may be initiated in “sub-threshold” fields of $\sim 0.3E_k$. We do not speculate here on the reasons for sub-threshold initiation; we use it only to mark where a sprite may be initiated. In such a case, the black curve in the fourth panel shows that initiation occurs on the axis above the discharge with a delay of 0.323 ms. For even higher thresholds, i.e., $0.6E_k$, again initiation occurs on-axis, albeit at a later time (but still within the first 1 ms; these are still “short-delayed” sprites). This time delay will depend on the peak current moment and the waveform shape.

[44] Now, the faster current, in the top panels, shows a very different structure. The snapshot at left shows that the maximum field occurs some distance away from the axis; since this simulation is axisymmetric, this maximum field forms a “ring” near 80 km altitude, with a radius (at this time step) of about 20–30 km. The second panel shows that on axis, the maximum field occurs at a similar time as for the slower current, but is not sustained for more than 0.2 ms; this shows that the maximum field is due to the EMP and induction fields, rather than the QE field. The third and fourth panels show that the maximum field at 78 km altitude occurs away from the axis. With our same threshold for sprite production at $0.3E_k$, initiation would occur at 78 km altitude, in a ring 20–25 km from the axis, 0.285 ms after the

discharge. At higher thresholds, the radius would be larger and the time delay greater.

[45] This mechanism explains how some sprites form in rings symmetric about the discharge axis. According to this model, ring sprites should be short-delayed sprites, due to very high peak currents which are discharged very rapidly. High time resolution imaging of sprites, together with detailed measurements of the source lightning current waveform, are required to verify or refute this mechanism.

6. Summary

[46] In this paper we have presented a new model of the lightning field interaction with the lower ionosphere. Maxwell’s equations and the Langevin equation are solved in a spherical coordinate system, to include the curvature of the earth, and nonlinear interactions are included such as heating, ionization, attachment, detachment, and optical emissions. 2D and 3D versions of the model have been developed. Any arbitrary source current can be included; as such, the model is applicable to studying both lightning and VLF transmitter signal propagation.

[47] We have presented three applications of this model. First, we investigated the effects of collisional electron detachment on the lightning-ionosphere interaction. We found that detachment plays a very small role in the first ~ 2 ms of the event; effects that are seen are predominantly associated with the enduring QE field due to the lightning charge moment. Second, we have used the new model to investigate elves observed from the ground by the PIPER instrument. In particular, we find that particular choices of lightning waveform parameters (rise and fall time) lead to the observed “elven doublets”. This result shows that PIPER observations can be used to determine parameters of the lightning waveform that cannot be measured by other

techniques. Finally, we have used the model to show that “ring sprites” may be initiated by fast, high-peak current discharges, due to the combination of QE and EMP fields having the maximum value of E_{eff}/E_k at some radius away from the discharge axis. Verification of this mechanism, however, requires high-speed observations of ring sprites, together with detailed measurements of the source current waveform.

[48] **Acknowledgments.** This work was supported by NSF CEDAR/GEM Postdoctoral Fellowship AGS-1027070, ONR grant N00014-09-0443, and DARPA grant HR0011-10-1-0058. The author thanks Supriya Chakrabarti for his support in obtaining this fellowship and Forrest Foust for proofreading this manuscript.

[49] Robert Lysak thanks the reviewers for their assistance in evaluating this paper.

References

- Barrington-Leigh, C. P. (2000), Fast photometric imaging of high altitude optical flashes above thunderstorms, Ph.D. thesis, Stanford Univ., Stanford, Calif.
- Barrington-Leigh, C. P., U. S. Inan, and M. Stanley (2001), Identification of sprite and elves with intensified video and broadband array photometry, *J. Geophys. Res.*, *106*(A2), 1741–1750.
- Becaache, E., S. Fauqueux, and P. Joly (2003), Stability of perfectly matched layers, group velocities and anisotropic waves, *J. Comput. Phys.*, *188*, 399–433.
- Béranger, J. P. (1994), A perfectly matched layer for the absorption of electromagnetic waves, *J. Comput. Phys.*, *114*, 185–200.
- Bilitza, D., and B. Reinisch (2008), International reference ionosphere 2007: Improvements and new parameters, *J. Adv. Space Res.*, *42*(4), 599–609, doi:10.1016/j.asr.2007.07.048.
- Chen, A. B., et al. (2008), Global distributions and occurrence rates of transient luminous events, *J. Geophys. Res.*, *113*, A08306, doi:10.1029/2008JA013101.
- Chevalier, T. W., U. S. Inan, and T. F. Bell (2008), Terminal impedance and antenna current distribution of a VLF electric dipole in the inner magnetosphere, *IEEE Trans. Antennas Propag.*, *56*(8), 2454–2468.
- Cho, M., and M. Rycroft (1998), Computer simulation of the electric field structure and optical emission from cloud-top to the ionosphere, *Jour. Atmos. Sol. Terr. Phys.*, *60*, 871–888.
- Cho, M., and M. J. Rycroft (2001), Non-uniform ionisation of the upper atmosphere due to the electromagnetic pulse from a horizontal lightning discharge, *J. Atmos. Sol. Terr. Phys.*, *63*, 559–580.
- Cooray, V. (1997), Energy dissipation in lightning flashes, *J. Geophys. Res.*, *102*, 21,401–21,410, doi:10.1029/96JD01917.
- Cummer, S. A., and W. A. Lyons (2004), Lightning charge moment changes in U.S. high plains thunderstorms, *Geophys. Res. Lett.*, *31*, L05114, doi:10.1029/2003GL019043.
- Cummer, S. A., and W. A. Lyons (2005), Implications of lightning charge moment changes for sprite initiation, *J. Geophys. Res.*, *110*, A04304, doi:10.1029/2004JA010812.
- Cummer, S. A., U. S. Inan, T. F. Bell, and C. P. Barrington-Leigh (1998), ELF radiation produced by electrical currents in sprites, *Geophys. Res. Lett.*, *25*(8), 1281–1284.
- Farges, T., and E. Blanc (2011), Lightning and the electric fields and their impact on the ionosphere, *C. R. Phys.*, *12*, 171–179.
- Farges, T., E. Blanc, and M. Tanguy (2007), Experimental evidence of region heating by lightning-induced electromagnetic pulses on mf radio links, *J. Geophys. Res.*, *112*, A10302, doi:10.1029/2007JA012285.
- Fukunishi, H., Y. Takahashi, M. Kubota, K. Sakanoi, U. S. Inan, and W. A. Lyons (1996), Elves: Lightning-induced transient luminous events in the lower ionosphere, *Geophys. Res. Lett.*, *23*(16), 2157–2160, doi:10.1029/96GL01979.
- Gordillo-Vázquez, F. J. (2008), Air plasma kinetics under the influence of sprites, *J. Phys. D*, *41*, 234016, doi:10.1088/0022-3727/41/23/234016.
- Gordillo-Vázquez, F. J., and A. Luque (2010), Electrical conductivity in sprite streamer channels, *Geophys. Res. Lett.*, *37*, L16809, doi:10.1029/2010GL044349.
- Hagelaar, G. J. M., and L. C. Pitchford (2005), Solving the Boltzmann equation to obtain electron transport coefficients and rate coefficients for fluid models, *Plasma Sour. Sci. Technol.*, *14*, 722.
- Haldoupis, C., R. J. Steiner, A. Mika, S. Shalimov, R. A. Marshall, U. S. Inan, T. Bosinger, and T. Neubert (2006), “Early/slow” events: A new category of VLF perturbations observed in relation with sprites, *J. Geophys. Res.*, *111*, A11321, doi:10.1029/2006JA011960.
- Hedin, A. E. (1991), Extension of the MSIS thermospheric model into the middle and lower atmosphere, *J. Geophys. Res.*, *96*, 1159–1172, doi:10.1029/90JA02125.
- Hu, W., and S. A. Cummer (2006), An FDTD model for low and high altitude lightning-generated em fields, *IEEE Trans. Antennas Propag.*, *54*, 1513–1522.
- Hu, W., S. A. Cummer, W. A. Lyons, and T. E. Nelson (2002), Lightning charge moment changes for the initiation of sprites, *Geophys. Res. Lett.*, *29*(8), 1279, doi:10.1029/2001GL014593.
- Inan, U. S., T. F. Bell, and J. V. Rodriguez (1991), Heating and ionization of the lower ionosphere by lightning, *Geophys. Res. Lett.*, *18*(4), 705–708.
- Inan, U. S., S. A. Cummer, and R. A. Marshall (2010), A survey of ELF and VLF research on lightning-ionosphere interactions and causative discharges, *J. Geophys. Res.*, *115*, A00E36, doi:10.1029/2009JA014775.
- Kopp, E. (1992), Positive and negative ions of the middle atmosphere, *Adv. Space Res.*, *12*(10), 325–333.
- Lawton, S. A., and A. V. Phelps (1978), Excitation of the $b^1\Sigma_g^+$ state of O_2 by low energy electrons, *J. Chem. Phys.*, *69*(3), 1055, doi:10.1063/1.436700.
- Lee, J. H., and D. Kalluri (1999), Three-dimensional ftd simulation of electromagnetic wave transformation in a dynamic inhomogeneous magnetized plasma, *IEEE Trans. Antennas Propag.*, *47*(7), 1146–1151.
- Li, J., S. A. Cummer, W. A. Lyons, and T. E. Nelson (2008), Coordinated analysis of delayed sprites with high speed images and remote electromagnetic fields, *J. Geophys. Res.*, *113*, D20206, doi:10.1029/2008JD010008.
- Liu, N. (2012), Multiple ion species fluid modeling of sprite halos and the role of electron detachment of O^- in their dynamics, *J. Geophys. Res.*, doi:10.1029/2011JA017062, in press.
- Luque, A., and F. J. Gordillo-Vázquez (2011), Mesospheric electric breakdown and delayed sprite ignition caused by electron detachment, *Nat. Geosci.*, *5*, 22–25.
- Marshall, R. A., and U. S. Inan (2010), Two-dimensional frequency-domain modeling of lightning-induced perturbations to VLF transmitter signals, *J. Geophys. Res.*, *115*, A00E29, doi:10.1029/2009JA014761.
- Marshall, R. A., U. S. Inan, and T. W. Chevalier (2008), Early VLF perturbations caused by lightning EMP-driven dissociative attachment, *Geophys. Res. Lett.*, *35*, L21807, doi:10.1029/2008GL035358.
- Marshall, R. A., U. S. Inan, and V. S. Glukhov (2010), Elves and associated electron density changes due to cloud-to-ground and in-cloud lightning discharges, *J. Geophys. Res.*, *115*, A00E17, doi:10.1029/2009JA014469.
- Mende, S. B., H. U. Frey, R. R. Hsu, H. T. Su, A. B. Chen, L. C. Lee, D. D. Sentman, Y. Takahashi, and H. Fukunishi (2005), D region ionization by lightning-induced electromagnetic pulses, *J. Geophys. Res.*, *110*, A11312, doi:10.1029/2005JA011064.
- Morgan, W. L., and B. M. Penetrante (1990), ELENDF: A time-dependent Boltzmann solver for partially ionized plasmas, *Comp. Phys. Comm.*, *58*(1–2), 127–152.
- Moss, G. D., V. P. Pasko, N. Liu, and G. Veronis (2006), Monte Carlo model for analysis of thermal runaway electrons in streamer tips in transient luminous events and streamer zones of lightning leaders, *J. Geophys. Res.*, *111*, A02307, doi:10.1029/2005JA011350.
- Nagano, I., S. Yagitani, K. Miyamura, and S. Makino (2003), Full-wave analysis of elves created by lightning-generated electromagnetic pulses, *J. Atmos. Solar Terr. Phys.*, *65*(5), 615–625.
- Neubert, T., O. Chanrion, E. Arnone, F. Zanotti, S. Cummer, J. Li, M. Füllekrug, S. Soula, and O. van der Velde (2011), The properties of a gigantic jet reflected in a simultaneous sprite: Observations interpreted by a model, *J. Geophys. Res.*, *116*, A12329, doi:10.1029/2011JA016928.
- Newsome, R. T., and U. S. Inan (2010), Free-running ground-based photometric array imaging of transient luminous events, *J. Geophys. Res.*, *115*, A00E41, doi:10.1029/2009JA014834.
- Pasko, V. P., U. S. Inan, T. F. Bell, and Y. N. Taranenko (1997), Sprites produced by quasi-electrostatic heating and ionization in the lower ionosphere, *J. Geophys. Res.*, *102*(A3), 4529–4561.
- Phelps, A. V., and L. C. Pitchford (1985), Anisotropic scattering of electrons by N_2 and its effect on electron transport, *Phys. Rev. A*, *31*(5), 2932–2949, doi:10.1103/PhysRevA.31.2932.
- Roden, J. A., and S. D. Gedney (2000), Convolution PML (CPML): An efficient FDTD implementation of the CFS-PML for arbitrary media, *Microwave Opt. Technol. Lett.*, *27*(5), 334–339.
- Rowland, H., R. Fernsler, J. Huba, and P. Bernhardt (1995), Lightning driven EMP in the upper atmosphere, *Geophys. Res. Lett.*, *22*(4), 361–364.
- Rowland, H. L., R. F. Fernsler, and P. A. Bernhardt (1996), Breakdown of the neutral atmosphere in the D region due to lightning driven electromagnetic pulses, *J. Geophys. Res.*, *101*(A4), 7935–7945.

- Stenbaek-Nielsen, H., R. Haaland, M. G. McHarg, B. A. Hensley, and T. Kanmae (2010), Sprite initiation altitude measured by triangulation, *J. Geophys. Res.*, *115*, A00E12, doi:10.1029/2009JA014543.
- Taranenko, Y. N., U. S. Inan, and T. F. Bell (1993), The interaction with the lower ionosphere of electromagnetic pulses from lightning: Heating, attachment, and ionization, *Geophys. Res. Lett.*, *20*(15), 1539–1542.
- Vadislavsky, E., Y. Yair, C. Erlick, C. Price, E. Greenberg, R. Yaniv, B. Ziv, N. Reicher, and A. Devir (2009), Indication for circular organization of column sprite elements associated with eastern mediterranean winter thunderstorms, *J. Atmos. Sol. Terr. Phys.*, *71*, 1835–1839, doi:10.1016/j.jastp.2009.07.00.
- Veronis, G., V. P. Pasko, and U. S. Inan (1999), Characteristics of mesospheric optical emissions produce by lightning discharges, *J. Geophys. Res.*, *104*(A6), 12,645–12,656.
- Wait, J. R., and K. P. Spies (1964), Characteristics of the Earth-ionosphere waveguide for VLF radio waves, *Tech. Note 300*, Natl. Bur. of Standards, Boulder, Colo.
- Yee, K. (1966), Numerical solution of initial boundary value problems involving maxwell's equations in isotropic media, *IEEE Trans. Antennas Propag.*, *14*(3), 302–307.

R. A. Marshall, Department of Electrical Engineering, Stanford University, 350 Serra Mall, Stanford, CA 94305, USA. (ram80@stanford.edu)